2013

TEMPORAL TRENDS IN GLOBAL SEA SURFACE TEMPERATURE FRONTS

Kelsey Marie Obenour
University of Rhode Island, kelsey_obenour@my.uri.edu

TEMPORAL TRENDS IN GLOBAL SEA SURFACE TEMPERATURE FRONTS

BY

KELSEY MARIE OBENOUR

A THESIS SUBMITTED IN PARTIAL FULFILLMENT OF THE

REQUIREMENTS FOR THE DEGREE OF

MASTERS OF SCIENCE

IN

OCEANOGRAPHY

UNIVERSITY OF RHODE ISLAND

2013

MASTER OF YOUR DEGREE THESIS

OF

KELSEY MARIE OBENOUR

APPROVED:

Thesis Committee:

Major Professor Peter Cornillon

Lew Rothstein

Gavino Puggioni

Nasser H. Zawia
DEAN OF THE GRADUATE SCHOOL

UNIVERSITY OF RHODE ISLAND
2013

ABSTRACT

Sea surface temperature (SST) fronts, generally defined as regions of enhanced surface temperature gradient, are of broad interest in oceanography both because of the role that they play in the dynamics of the upper ocean and because of the large volume of data available from satellite-borne sensors with which they can be studied. Gradients in the background surface temperature, surface wind stress, and cloud cover likely play a role in establishing and maintaining SST fronts. Furthermore, each of these characteristics is thought to be affected by changes in global climate. The objective of this study is to determine to what extent the probability of finding SST fronts in satellite-derived SST has changed in the recent past. To this end, front probability was determined from the output of an edge detection algorithm applied to the 30-year (1981-2011) time series of Pathfinder v5.2 SST data.

Based on approximately 1°x1° squares that are 90% or more clear, front probability has been found to increase globally at a very nearly linear rate of approximately 0.25 %/decade; i.e., over the 30-year period the mean probability of finding a front has increased from approximately 5.58% to 6.30%. However, the trend in front probability is not globally uniform so the study also included a determination of regional trends in front probability. Requiring broad temporal coverage in each 1°x1° square, to reduce the uncertainty associated with the trend estimates, resulted in dense coverage only in an approximately 750 km wide 'coastal' band. In this region, clusters of predominantly positive trends that were significantly larger, 0.6 to 0.8 %/decade, than the mean trend were observed; i.e., increases of 30 to 50% in the number of fronts over the past 30 years. The mean trend in the 'coastal band' is

approximately 0.30%/decade, substantially higher than the global trend. This implies that the increase in front probability in coastal regions is significantly larger than in open ocean regions.

ACKNOWLEDGMENTS

This thesis would not have been possible without the guidance, motivation, patience, and enthusiasm of Peter Cornillon. He is a wonderful advisor, teacher, and scientist. I am also grateful to Lew Rothstein and Gavino Puggioni for their knowledge and input as committee members. Thanks to Jason Dahl for serving as the committee chairperson.

I am indebted to my many colleagues who supported and sparked my research interests. Thank you to those who inspired my interest in oceanography early on as a SURFO: Christian Buckingham, Rob Pockalny, and Kathy Donohue. I'd like to acknowledge my funding sources, which are NASA and the URI OCG 200 and 506 teaching assistantships.

I am exceptionally grateful for the support of my family and close friends. My mother is always there for support and empathy. My father instilled a determination and drive in me at a young age that helped me persevere through difficult classes and research tasks. My sister has always given me inspiration and always knew what I needed before I did. I extend a deep gratitude to my grandmother who is looking down on me now; she always had faith in my ability to complete my masters. A tremendous appreciation goes to my patient and understanding boyfriend who stood by me during overwhelming times in the past year. A special thanks goes to my friends in Rhode Island that acted as an adventurous and supportive family away from home.

PREFACE

Rather than using the traditional division of the thesis into chapters, this thesis is written in “manuscript" style. The main text is written in a manner appropriate for submission to a scientific journal.

TABLE OF CONTENTS

LIST OF TABLES

TABLE **PAGE**

LIST OF FIGURES

FIGURE **PAGE**

Manuscript

Temporal Trends in Global Sea Surface Temperature Fronts

by

Kelsey M. Obenour[1] and Peter C. Cornillon[1]

Formatted for submission to the Journal of Geophysical Research - Oceans

[1] Graduate School of Oceanography, University of Rhode Island, Narragansett, Rhode Island, USA.

Corresponding author: kelsey_obenour@my.uri.edu

Corresponding author: kelsey_obenour@my.uri.edu

[2] This problem will be addressed in the next version of Pathfinder processing due to be

MANUSCRIPT

Temporal Trends in Global Sea Surface Temperature

1.1 Introduction

Ocean fronts separating water masses of different properties are abundant throughout the upper ocean. Not only do they delineate water masses, but they are also thought to play an important role in a broad range of ocean processes. The atmosphere and the ocean form a coupled system, exchanging heat, momentum, and water at the air-sea interface. Air-sea interactions in frontal regions are particularly pronounced because of changes in stability of the marine atmospheric boundary layer across the front (Chelton et al. 2001; Liu et al. 2000; Song et al. 2006; Small et al. 2008). The result is a complicated set of feedback processes affecting both the ocean and the atmosphere. Given their importance in air-sea interactions, it is not surprising that fronts are being implicated in climate processes as well, specifically, ocean fronts are thought to act as "the duct through which heat, carbon, oxygen, and other climatically important gases enter into the deep ocean" (Ferrari, 2011). But fronts are also important in climate dynamics because of the role that they play in mixing – recent observational and numerical studies have found that fronts are very active in the exchange of energy between the mesoscale and the micro-scale, the scale at which dissipation takes place in the ocean (D'Asaro et al., 2011; Fox-Kemper et al., 2011; Molemaker et al., 2010; Thomas et al., 2008; Capet et al., 2008).

Ocean fronts are also recognized as a major player in marine ecosystems and bio-productivity (Le Fevre, 1986; Olson et al., 1994; Longhurst, 2010). One of the primary mechanisms, but not the only one, giving rise to these biological effects is

surface convergence toward the front. Such convergences contribute to elevated primary production at the frontal boundary resulting in ‘‘hot spots” of marine life, from phytoplankton to apex predators, hot spots that are recognized as being spawning, nursing, and feeding areas for fish, sea birds, and marine mammals, with high biodiversity (Belkin et al., 2009).

Fronts may be associated with any ocean parameter but particular attention is devoted to sea surface temperature (SST) fronts for several reasons. First, in many cases fronts are readily identified by their temperature signature; i.e., dynamical fronts in the upper ocean generally coincide with SST fronts. Second, important dynamics are associated with large temperature gradients in the ocean, especially as relates to air-sea processes. Third, global SST fields at moderately high spatial (1-10 km) and temporal (twice daily, clouds permitting) resolutions dating back to 1981 allow for global studies of the distribution and evolution of SST fronts.

A number of physical processes are thought to play a role in the formation, enhancement, and maintenance of SST fronts with wind, solar insolation, and background temperature gradients generally contributing either directly or indirectly. Solomon et al. (2007) found that each of these is changing as a result of anthropogenic inputs of greenhouse gases. Furthermore, the temporal trends in these properties appear to vary geographically (Norris, 2005 for clouds; Young et al., 2011 for winds; Merchant et al., 2012 for SST). It is therefore likely that the frequency of fronts is changing as well and that these changes vary geographically. To date there has only been one published study that we are aware of that has looked at changes in front probability and this only for a fairly small region in the California Current System

(Kahru et al., 2012). The present study was undertaken to extend the work of Kahru et al. (2012) to all regions in the global ocean sufficiently clear to obtain reliable estimates of the change in front probability as well as to address a set of problems with the SST dataset that were uncovered during the course of this work. Although the approach presented herein is similar to Kahru et al., it is not identical. Differences will be discussed where appropriate and our results will be compared with those of Kahru et al. (Section 1.3.1).

In the next section we discuss the edge detection algorithm used for this analysis. This is followed by a discussion of the data, of how front probability is determined from the time series and of the corrections made to the Pathfinder time series to address issues likely to impact front probability. The results are then presented and discussed. We close with a brief summary of the results.

1.2 Methodology

1.2.1 Front Detection: SIED

Front edge detection algorithms fall between two extremes: population-based and gradient-based. Population-based algorithms identify fronts as lines that separate two or more populations within a region, typically 16 pixels or larger in each dimension. Gradient-based algorithms generally convolve a much smaller kernel, order 1 to 3 pixels in each dimension, with the SST field and then threshold the resulting gradient field to obtain the location of fronts. Front pixel identification is well defined in the population-based algorithms but is problematic in gradient-based algorithms. An advantage of population-based algorithms is that they reliably identify relatively weak fronts associated with large water masses while avoiding the clutter of weak fronts associated with small regions. Gradient-based algorithms do not distinguish between weak fronts associated with large water masses and those associated with small regions. In this study the Single Images Edge Detection (SIED) algorithm developed at the University of Rhode Island is used to identify fronts. Kahru et al. (2012) also used this algorithm for their study. Following is a brief overview of the SIED algorithm. For a more detailed description of the algorithm the reader is referred to Cayula and Cornillon (1992, 1995).

The SIED algorithm is based on statistical analysis of histograms of SST values in 32x32 pixel windows of the SST image. The algorithm searches for two distinct populations in each region, a warm population (A) and a cold population (B), that meet a set of criteria based on the characteristics of the two distributions; e.g., the separation of the mean SST values of the pixels in the two populations. It then

examines the populations for cohesion. Cohesion is a measure of how close (spatially) pixels in population A are to one another compared to pixels in population B. A checker-board pattern, which would have two very narrow peaks, one corresponding to the temperature of the white squares, say the A population, and the other to the temperature of the black squares, the B population, would have low cohesion, while a region with pixels in one population, lying to the north of a given line, the A population, and pixels in the other population to the south of the line, the B population, would have the maximum cohesion possible. If the data is cohesive the two populations are assumed to represent different water masses. The SIED algorithm then descends to the pixel level and uses a contour following algorithm to identify additional pixels associated with the front. As its name implies, the SIED algorithm operates on individual images.

Front data are available after a single pass of SIED over a time series of SST fields. However, a second pass of the algorithm (Cayula and Cornillon, 1995), following merging and thinning of fronts found in the first pass, will result in an increase in the number of front pixels identified in the dataset in regions where cloud cover has reduced the number of pixels in the histogram to a point where two populations could not be reliably found. For the analysis performed here this two-pass approach was used. Fronts were merged for all images within a plus/minus 48-hour interval of the image of interest, excluding fronts found in that image. The output of this step is a field of zeros where there were no fronts in adjacent images and ones where a front was found. Regions consisting of a number of adjacent front pixels were then thinned to lines that are only one pixel wide. The thinning is performed based on

the local SST gradient. These lines are then used as seeds in the contour following portion of the SIED algorithm in the second pass – along with the seed pixels that the algorithm finds on the image of interest.

There are several thresholds that are important when identifying fronts using the SIED algorithm. As configured, the SIED algorithm required at least 100 clear pixels within a 32x32 pixel region and the smaller of the two populations found in the histogram analysis must have at least one quarter of the total number of clear pixels in the region. The mean of the warm population must be 4 or more digital counts larger than the mean of the cold population. SST in the Pathfinder v5.2 dataset are sampled at 0.01K, but for this study they were resampled at 0.05 K – well below the 0.4 K accuracy associated with the dataset – to facilitate manipulation of the histograms. At 0.05 K per digital count the minimum separation of 4 digital counts corresponds to a separation of 0.2 K between the means of the warm and cold populations. Finally, frontal segments were required to be at least five pixels long. The algorithm will not find a front if these thresholds are not met.

1.2.2 Data

Two satellite-derived SST datasets were used in this study, one obtained from the Advanced Very High Resolution Radiometers (AVHRR) carried on the National Oceanographic and Atmospheric Adminstration's (NOAA) series of operational polar orbiting satellites and the second from the Spinning Enhanced Visible and InfraRed Imagers (SEVIRI) carried on the European Meteosat Second Generation (MSG) satellite series. The AVHRR data, which provide global coverage from November 1981 to present, were used to determine trends. The SEVIRI data, covering only the hemisphere centered on the prime meridian from June 2003 to present, were used to address the problem of orbital drift associated with NOAA's polar orbiting satellites (Section 1.2.4.1).

Pathfinder v5.2 SST data, the AVHRR-based dataset, are available on a 0.0417° Plate-Carré grid with nearly complete global fields every 12 hours, one corresponding to the local sun time of the ascending equatorial crossing of the satellite carrying the sensor, the daytime field, and the other corresponding to the descending equatorial crossing, the nighttime field. Coverage of this dataset extends from November 1981 through December 2011. Details of the Pathfinder SST retrieval algorithm are available in Kilpatrick et al. (2001) with additional details available at the NOAA website, http://www.nodc.noaa.gov/sog/pathfinder4km/, from which the data may also be obtained.

A quality level, ranging from 0 (worst) to 7 (best), was assigned to every pixel for which the sensor collected data and there was a corresponding SST value for that location, albeit likely a meaningless value for those locations of very low quality.

Locations for which there was no data were assigned a value of -1. The criteria for assigning quality values to a given pixel are based on one or more tests. Of particular concern with regard to front detection is that one of the criteria used is based on the local variance of radiance at the pixel location with pixels that fail this test being assigned a relatively low value. If the high variance in radiance resulted from an SST front, this pixel, which may in fact have been clear, would be assigned a low quality. Unfortunately, these quality values were also associated with other tests, which in general corresponded to data of low quality. This makes selecting the quality threshold to use in selecting 'good' retrievals problematic at best – selecting all quality values equal to or above this low level would result in many poor retrievals being included in the data to be processed, which in turn might result in false fronts or difficulty in finding fronts, while setting the threshold above this value would result in high gradient regions, i.e., strong SST fronts, being rejected. Although it may be possible to address this by 'unmasking' pixels that are clearly related to fronts, the problem is further complicated by the fact that the assignment of quality levels for Pathfinder v5.2 inadvertently assigned a -1 to SST values for pixels of poor quality; i.e., rather than simply flagging the pixel as low quality but retaining the retrieved SST value, a value of -1 was recorded[2]. The result is that strong fronts are often flagged as bad data with no possibility to retrieve the actual SST value at that location. This problem applies to the entire 30 year time series analyzed here hence is not expected to contribute significantly to the trends identified in the analysis. With the above observations in mind, a quality threshold of 4 was selected for this study, pixels with a

[2] This problem will be addressed in the next version of Pathfinder processing due to be complete by early 2014.

quality level of 3 or less were flagged as bad and not used in the histogram analysis of the SIED.

There are some other issues with regard to the Pathfinder v5.2 time series that are relevant to the analysis presented herein. To begin with, there are spatial and temporal gaps in the time series. The most significant of these is a gap between the failure of NOAA-13 following launch in September 1994 and its replacement with NOAA-14 in January 1995. This gap is evident in Figure 1 showing the monthly sum of clear pixels as a function of latitude. There is also a problem with the early NOAA-14 data at high latitudes, greater than 40°N and 40°S. This problem seems to have been resolved by early 1996 at most latitudes, but not north of about 70°N. There are virtually no clear pixels above 75°N, and only a small number between 70° and 75°N, from January 1995 through at least 2005 while prior 1995, there was a significant number of pixels every year in this region. The reason for this is unknown.

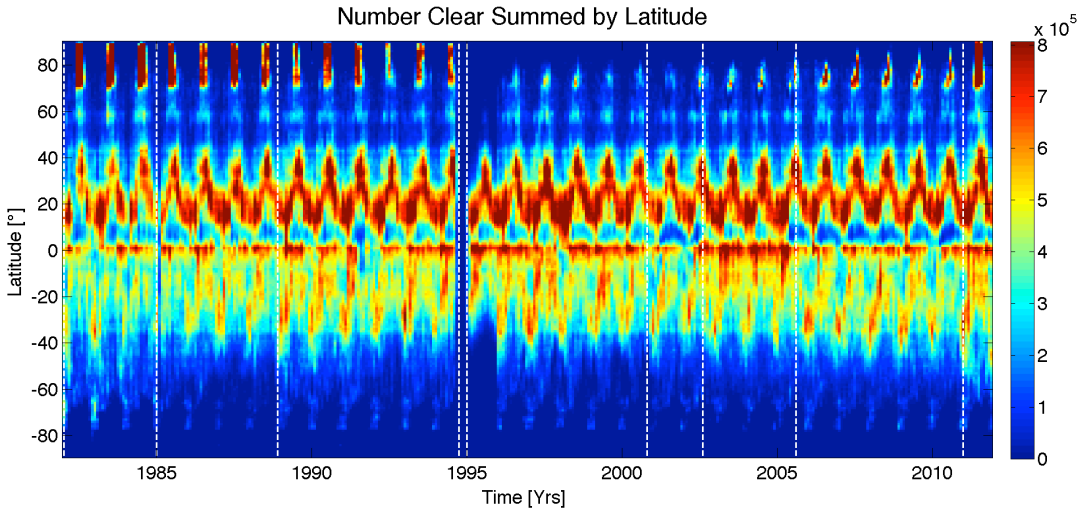

Figure 1. Monthly sum of clear pixels by latitude. Vertical dashed white lines correspond to the dates when there was a change in the satellite from which the data were obtained.

Because of the significant difference in front probability for some locations throughout the course of the day (discussed in more detail in Section 1.2.4.1) and because of the known creation and elimination of fronts during the day due to diurnal warming (Salter, 2013), only nighttime fields were used in the global and regional analyses discussed in Section 1.3.2 and 1.3.3. The nighttime probability of a clear pixel at each pixel location for the 30-year times series analyzed here is shown in Figure 2. This field was obtained by dividing the sum of clear pixels (quality 4 or greater) at each pixel location in the Pathfinder v5.2 SST time series by the number of nighttime fields in the time series[3]. Note the relatively low probability of finding a clear nighttime pixel in the Gulf Stream region. We believe that this is related primarily to the radiance variance test discussed above

The other dataset used in this study is based on the SEVIRI instrument carried on the MSG satellites. MSG spacecraft are flown in a geostationary orbit centered on the Prime Meridian at the Equator hence they collect detailed imagery of the hemisphere centered on the intersection of the Prime Meridian and Equator. Spatial resolution ranges from a little under 4 km at nadir to O(6-km) over the Mediterranean, the western Atlantic and even larger values at high latitudes. Although the sensor scans the hemisphere every 15 minutes only hourly fields were used for this study.

[3] This is actually an estimate of the probability in that some fields may be incomplete, either because of missing orbits or regions not covered in the nightly composite (equatorial regions); i.e., these probabilities tend to be a slight underestimate of the actual probability.

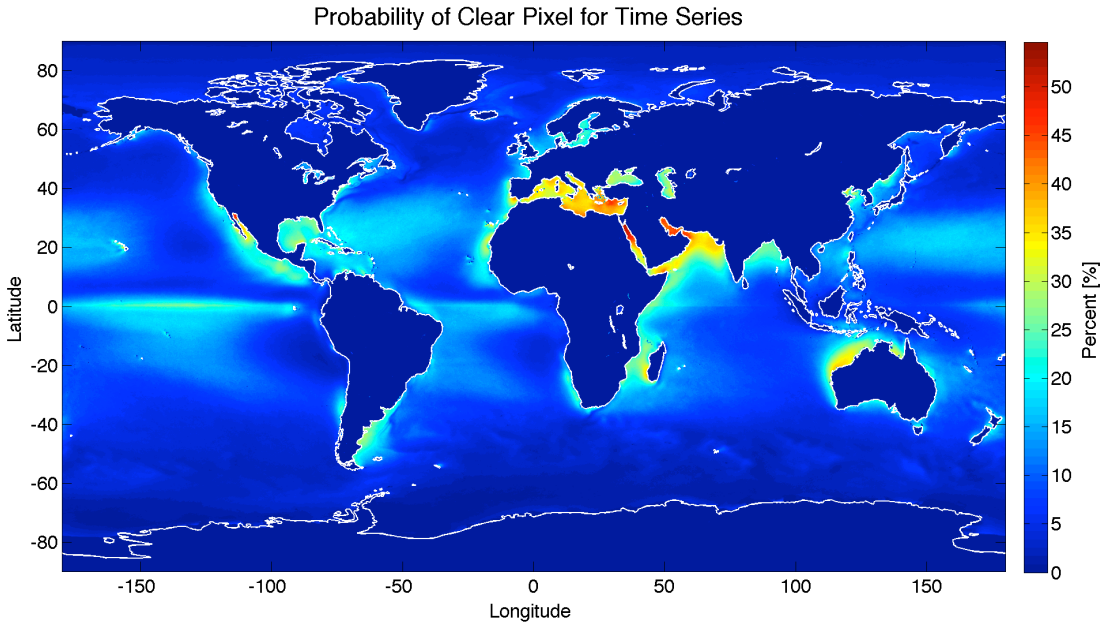

Figure 2. Probability that a pixel is cloud free, calculated by dividing the sum of clear night pixels by the number nights in the time series.

1.2.3 Front Probability

Front probability is defined as the total number of front pixels in a space-time window divided by the total number of clear pixels in the same window. To provide a reference from which to interpret the trends in SST front probability, nighttime front probability for the 30-year study period is presented in Figure 3. As suggested by the large values and the significant variability, values above 80°N are suspect and so we will therefore not estimate trends in front probability in this region.

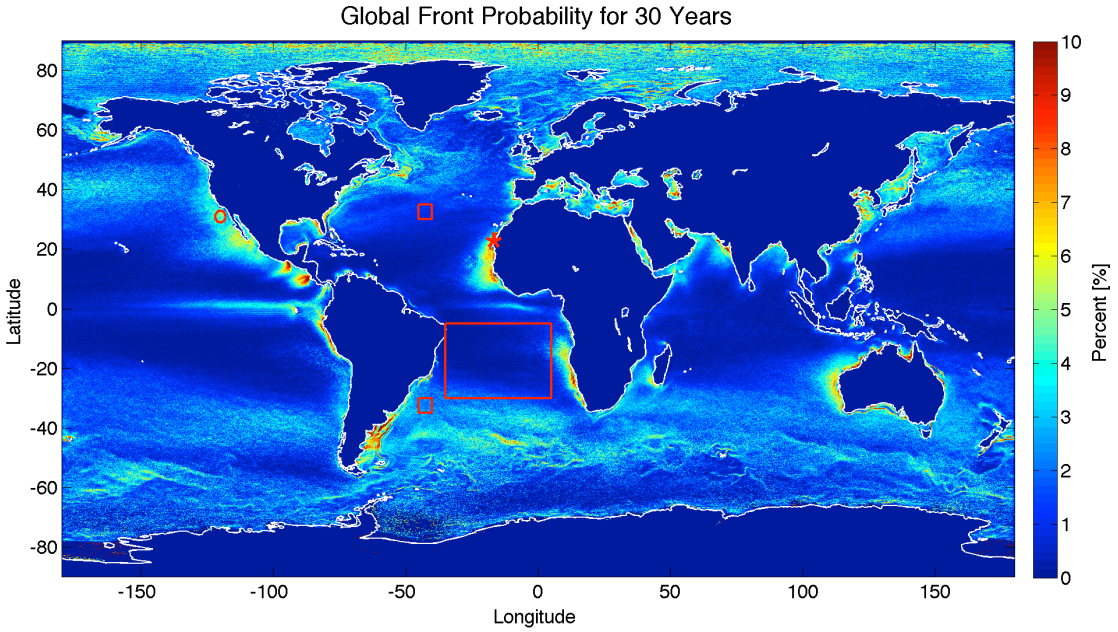

Figure 3. Global front probability at each Pathfinder pixel location. Small square boxes in the North and South Atlantic are used in section 1.2.4.1 to provide an estimate of the diurnal variability in front probability. The large square in the South Atlantic is used in section 1.2.4.2 to examine SST variability that might be associated with sensor noise. The small circle off the coast of California shows the Ensenada Front area studied by Kahru et al. (2012) and discussed in section 1.3.1. The star in the North Atlantic off the coast of Africa is the location from which the example of a front probability time series discussed in section 1.3.3 was drawn.

For each time series of front probability, a temporal trend was determined by least squares fitting a straight line to the time series. The spatial extent of the space-

time window used to estimate front probability was chosen to correspond to alternate 32x32 pixel squares used by the SIED algorithm to identify fronts while the temporal extent was chosen to be one month. The SIED algorithm performs an analysis on the first 32x32 pixel region in the image and then steps 16 pixels eastward and repeats the analysis. When the first row is complete, the algorithm returns to the western side of the image and steps southward by 16 pixels and repeats the process. Every other 32x32 pixel window and every other row of such windows was used for the regional trend analyses. We refer to these 32x32 pixel regions as SIED windows in the following.

1.2.4 Corrections to be made to Pathfinder Time Series

In this section we discuss issues that may result in trends in front probability that are not real, but rather an artifact of the satellite or processing.

1.2.4.1 Orbital Drift

NOAA satellites carrying the AVHRR instruments are in sun-synchronous, 'polar' orbits. Although the orbits remain very nearly sun synchronous, their equatorial crossing times drift slowly over the life of the satellite. In that front probability changes over the course of the day, care must be taken to address the possible impact of "orbital drift" on the trends obtained from the time series. Data from the AVHRRs carried on NOAA-7, 9, 11, 14, 16, 17, 18, and 19 comprise the Pathfinder v5.2 time series (Evans, 2013). All but NOAA-17 have early afternoon ascending (northward) equatorial crossing times[3], with NOAA-7 and -9 at ~1430, NOAA-11 and -14 at ~1330, and NOAA-16, -18, and -19 at ~1400 (Ignatov and Laszlo, 2004). These orbits descend back from north to south on the dark side of the Earth 12 hours later. NOAA-17 has an ascending equatorial crossing time of ~2200, with the descending crossing time of ~1000. These are the targeted times of the ascending nodes at launch but as noted above, the actual crossing times drift over the lifetime of the satellite as shown in Figure 4 (Ignatov and Laszlo, 2004). Note that these satellites were in orbit beyond, and in some cases before, the times shown in Figure 4; only the period for which the data were used in the Pathfinder time series are shown here. As a result, this plot also serves to show which satellites contribute to the time series and when.

[3] In this manuscript, equatorial crossing times are given as local sun time.

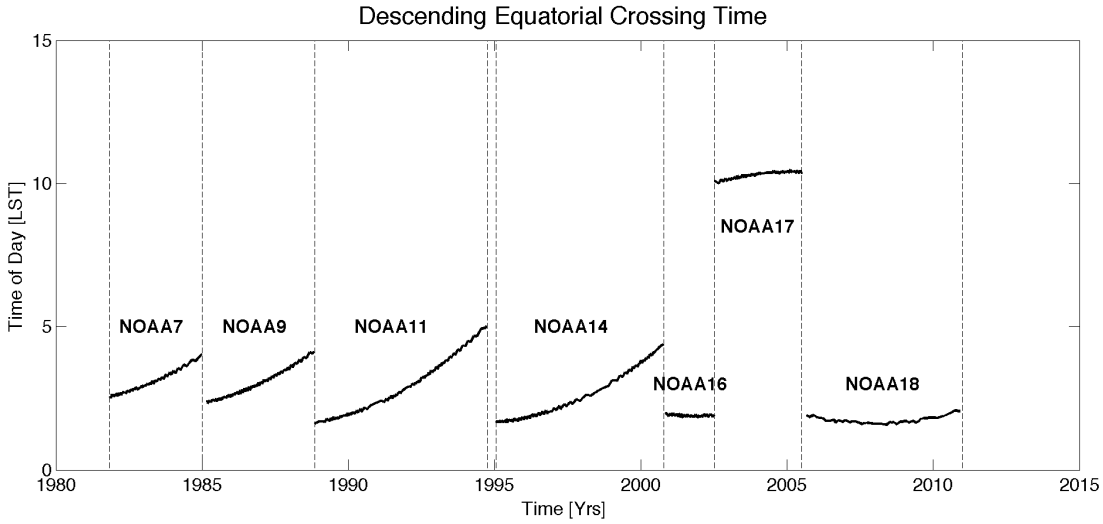

Figure 4. Descending equatorial crossing times for the satellites used in the Pathfinder v5.2 dataset. Vertical dashed lines correspond to the dates when there was a change in the satellite from which the data were obtained.

Since satellites drift over time, it is important to consider how front probability changes over the course of a day. Figure 5 illustrates the mean MSG front probability for June 2004-February 2011 as a function of time of day for two 5°x5° squares, one in the North Atlantic and the other in the South Atlantic (see Figure 3 showing the locations of these regions). Also shown in Figure 5 is the mean Pathfinder front probability for the same period. The Pathfinder means are shown as horizontal lines, the extent of which indicates the approximate time of day of the data contributing to these means. The slightly lower front probability of the Pathfinder data compared with the MSG data likely results from the slightly lower signal to noise ratio of the Pathfinder data; the regions for which these statistics were calculated were chosen so that the spatial resolution is similar for both data datasets.

The cause of the rather significant peak in front probability in the middle of the afternoon is the subject of an ongoing study and is not precisely understood at present.

However, for the purpose of this study it is clear that, at least at some locations, there is a strong diurnal signal in front probability with the most rapid changes occurring at mid-day and early evening and relatively little variability from late evening to sunrise. Knowing how the diurnal signal varies geographically and as a function of time of year would allow for a correction of the Pathfinder front probabilities for orbital drift. However, these data are not available globally so for all but the comparison of our results with those of Kahru et al. (2012), discussed in Section 1.3.1, we use only the nighttime data front probabilities to estimate trends. Furthermore, as will be discussed in more detail below, we exclude data obtained from NOAA-17 from the global analyses because of the substantial difference in time between the equatorial crossing of NOAA-17 and those of the other satellites in the series.

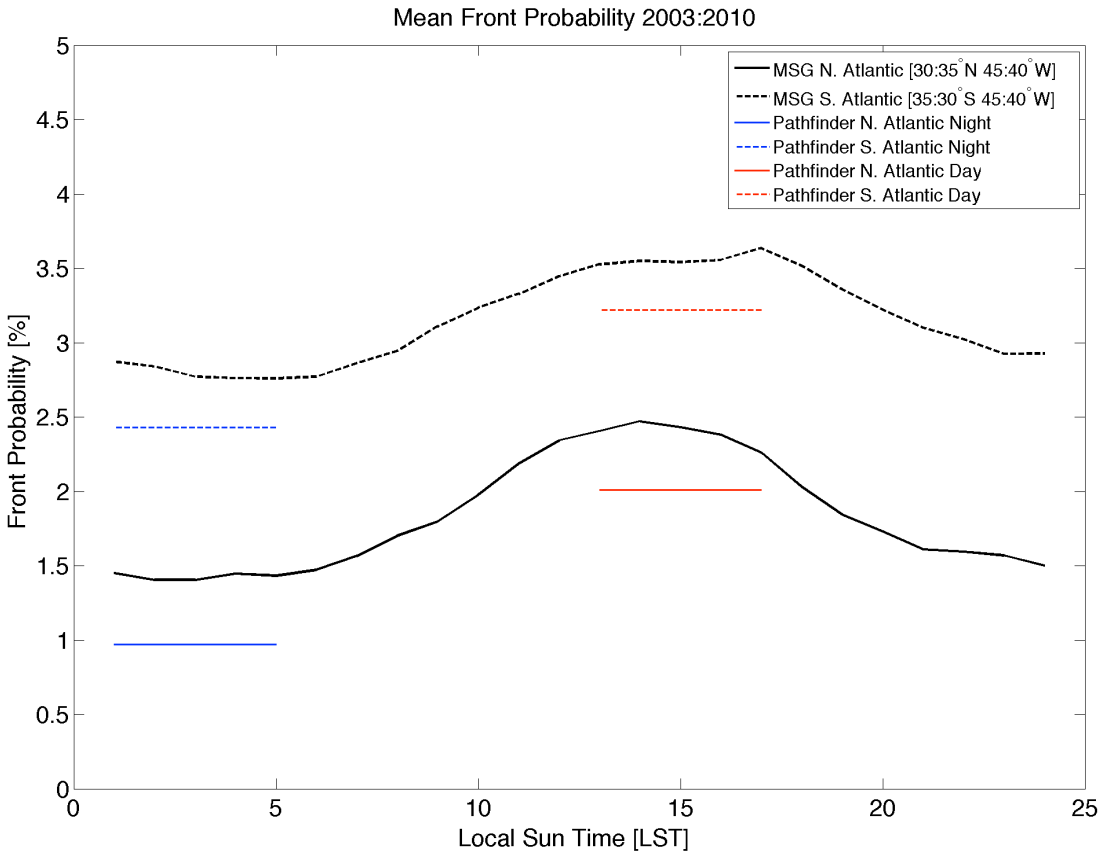

Figure 5. Mean front probability from MSG is shown as a function of time of day for two regions, the dashed line for a 5°x5° square in the South Atlantic (35-30°S and 45-45°W) the solid line for one in the North Atlantic (30-35°N 45-40°W). The horizontal lines represent the front probability obtained from Pathfinder v5.2 for the same regions and time period.

1.2.4.2 Sensor Characteristics

Front probability, determined with the SIED algorithm, depends on noise in the SST field (Cayula and Cornillon, 1992). In order to minimize the impact of noise on front detection, the data were median filtered with a 3x3 pixel filter prior to the application of the SIED algorithm. However, despite the median filtering of the data, changes in the characteristic of the sensors used in the Pathfinder v5.2 time series as well as degradation of the sensors while on orbit could lead to trends in sensor noise that would contaminate trends in front probability. To determine whether or not this is a problem, the mean 3x3 pixel variances of the median filtered SST data were averaged for each SIED window in each nighttime image. The mean variance of these variances for the 30-year time series was then obtained and plotted (not shown). An area of the South Atlantic (5-30°S, 35°W-5°E; indicated in Figure 3) showed the smallest average variance globally. The time series for this region is shown in Figure 6. This region was chosen to minimize the contribution of geophysical noise to the variance – the variance of interest here is that resulting from noise in the instrument and/or noise in the retrieval, but not in oceanic or atmospheric variability. The trend in SST spatial variance over the 30-year study period (Table 1), $5.0 \times 10^{-5} \pm 2.6 \times 10^{-5}$ K^2/year, is not statistically different from zero at the 95% confidence level although just barely so. However, excluding the NOAA-14 data in 1995 and all NOAA-17 data, for reasons indicated below, results in a drop of the trend to $1.3 \times 10^{-5} \pm 2.8 \times 10^{-5}$ K^2/year, which is clearly not significant, hence is unlikely to contribute significantly to trends in front probability. Furthermore, none of the trends of the individual satellites (Table 1) is significantly different from zero at the 95% confidence level suggesting that

sensor degradation if any does not play a significant role in front probability trends for the individual satellites. However, the mean of the variances for the data from NOAA-17 is significantly lower (more than 5 standard deviations) than those of the data obtained from the other satellites (Table 1). The reason for this is not known. Given the low variance and the fact that the equatorial crossing time of NOAA-17 also differs substantially from those of the other satellites, NOAA-17 (July 2002 and July 2005) data will be excluded from global and regional analyses of trends in front probability. We note, as an aside, that the variance of the data in this region suggests that the spatial precision – the pixel-to-pixel noise – of Pathfinder 3x3 median filtered nighttime retrievals is less than approximately 0.17 K.

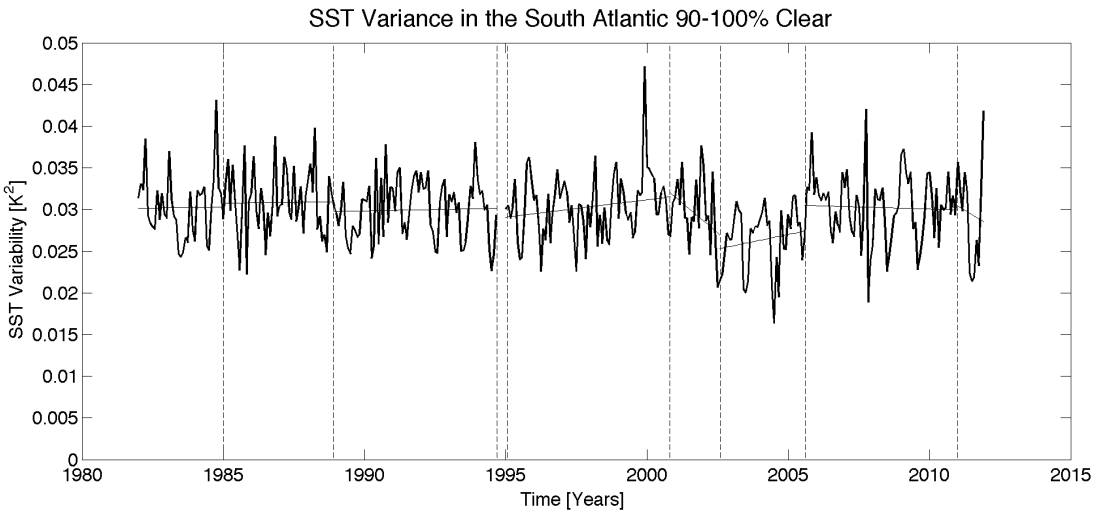

Figure 6. The monthly mean SST variance on 3x3 pixel squares in the South Atlantic (5-30°S, 35°W-5°E).

	Slope (K^2/year x10^{-5})	Standard Deviation of the Slope (K^2/year x10^{-5})	χ^2	Reject Hypothesis for normalcy	Mean Variance (K^2)	Standard Error of the Mean (K^2)
NOAA-7	0.33	6.75	8.7	Yes	0.030	0.00065
NOAA-9	0.31	4.16	5.5	No	0.031	0.00057
NOAA-11	0.53	2.15	7.1	No	0.030	0.00042
NOAA-14	6.02	3.10	5.3	No	0.030	0.00052
NOAA-16	-15.98	16.07	0.7	No	0.030	0.00089
NOAA-17	5.79	4.95	5.7	No	0.026	0.00070
NOAA-18	-1.34	2.37	3.3	No	0.030	0.00051
NOAA-19	-16.94	68.78	0.4	No	0.030	0.00190
Time Series	-0.41	0.21	5.1	No	0.030	0.00022
Abbreviated Time Series	-0.11	0.22	9.9	No	0.030	0.00021

Table 1. Statistics for SST variance in the South Atlantic by satellite. Column 2 – the trend in variance for the given satellite; column 3 – the standard deviation in the trend of column 2; column 4 – the chi squared value of the fit associated with these data; column 5 – whether or not the hypothesis that the residuals following the straight line fit to the data are normally distributed, 'No' means that the hypothesis can not be rejected, i.e., a straight line fit to the data is reasonable; column 6 – the mean of the variances for the given satellite, and; column 7 – the standard error of the mean of column 6.

1.2.4.3 Percent Cloud Cover in SIED Windows

Next, we consider the possible impact of a possible trend in the fraction of cloud cover. Such a trend could contribute to a trend in front probability in two ways. First, there could be a geophysical correlation between fronts and clouds. This could come about in one of two ways: (1) a large change in SST across fronts may result in a modification of the marine atmospheric boundary layer, which may in turn result in a change in cloud cover (Park et al., 2006) that obscures the front – or at least the pixels that are flagged as cloud-contaminated (the cloud mask often extends one or two pixels beyond the actual cloud edge) – or (2) heavy clouds associated with an atmospheric front may result in differential warming of the surface that presents as an ocean front as the cloud moves away from the region.

The second general category of potential trends in front probability resulting from clouds is associated with the SIED algorithm. Front probability is calculated by dividing the number of times a pixel was marked as a front pixel by the number of times that that pixel was clear for the same space-time window (Ullman and Cornillon, 1999). Ideally this should correct for the presence of clouds, resulting in a frontal probability that remains constant independent of the frequency of cloud cover in the space-time window. However, Howe et al. (2013) found that front probability, derived from satellite data using the SIED algorithm, was significantly lower than front probability obtained from model data, which were unobstructed by clouds. They attributed this to several factors associated with the algorithm. First, if less than approximately 10% of the pixels in a histogram are present or if one of the two populations found comprise less than one quarter of the clear pixels – e.g., the front, if

one exists, is near the edge of the 32x32 pixel window – the algorithm does not attempt to find a front but the clear pixels that are present are included in the clear count. This error depends only on the fraction of clear pixels in the window. Second, scattered clouds may block the contour following portion of the algorithm. This will result in less front pixels being found than would be found in a cloud-free version of the field in two fashions. Pixels that may have been identified as front pixels beyond the missing value that is blocking the contour are not counted and, second, the number of pixels prior to the blockage may fall below the 5 pixel threshold and again are not counted. This error depends on the fraction of clear pixels *and* on the cohesion of the pixels in that small, scattered clouds are more likely to block contours than large clouds covering the same fraction of the window.

To evaluate the effect of percent cloud cover on the performance of the SIED algorithm, the front probability determined from each of the sixteen 32x32 SIED windows covering an approximately 5 degree square of the North Atlantic (30-35ºN 45-30ºW) was plotted as a function of the percent of a given SIED window that was clear (Figure 7). This plot supports the findings by Howe et al. (2013) that front probability is a strong function of the fraction of valid pixels in each SIED window despite the attempt to normalize for cloud cover. To avoid trends that might result from a change in the fraction of cloud cover over time, trends in front probability are determined only for SIED windows that are at least 90% clear.

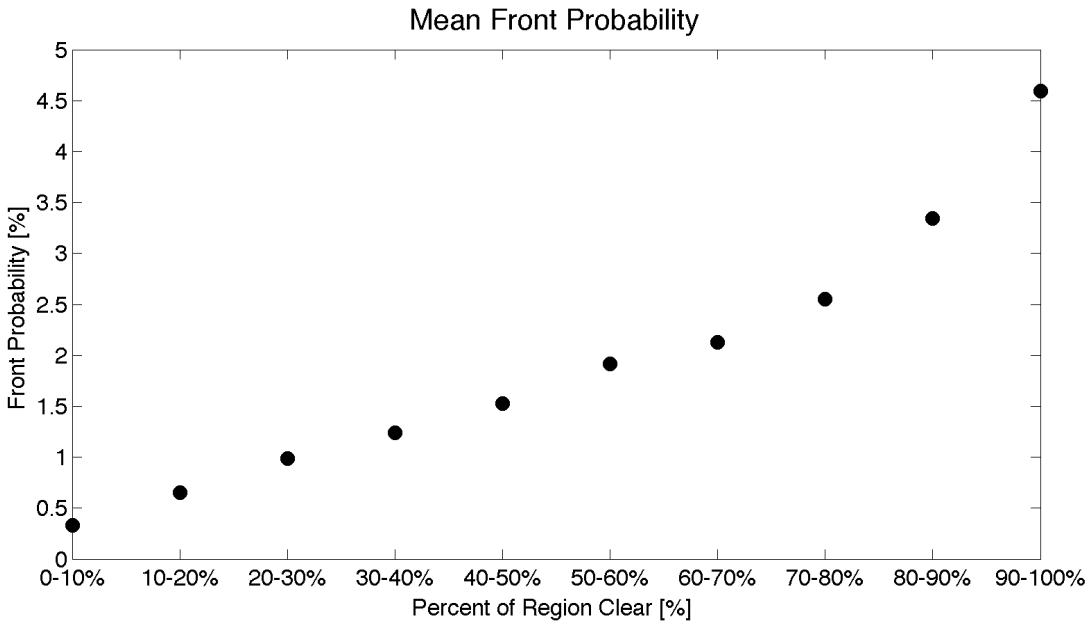

Figure 7. Mean front probability as a function of percent clear of a 32x32 pixel window.

Although limiting the analysis to SIED windows that are at least 90% clear limits the impact of cloud cover on SIED front probability, the steep slope in front probability as a function of cloud cover between 70 to 80% clear and 90 to 100% clear (Figure 7) suggests that a trend in cloud cover could still impact the trend in front probability. To determine whether or not this is a problem the monthly time series of fraction clear was developed for all SIED windows that are at least 90% clear in the same North Atlantic (30-35ºN 45-30ºW) region (Figure 8). The slope of this time series is 0.013% per decade with a standard deviation of 0.19% per decade. The trend is not significantly different from zero at the 95% confidence level hence is not expected to contribute to a trend in front probability.

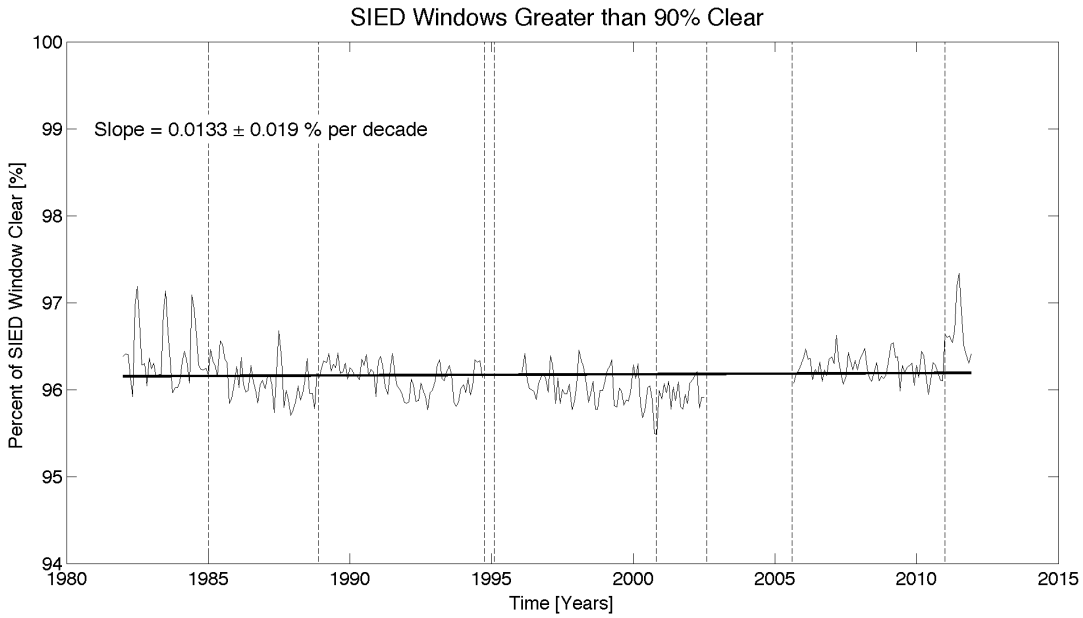

Figure 8. Mean front probability for SIED windows that are at least 90% clear.

1.3 Results and Discussion

Global and window level analyses were conducted on Pathfinder v5.2 data to determine both the global trends in front probability and the geographic variability in these trends. In addition, a regional analysis was performed for a small area in the California Current System (CCS) for comparison with the results of Kahru et al. (2012). These analyses are discussed in depth below.

1.3.1 The Ensenada Front

Kahru et al. (2012) quantified trends in front probability in the CCS. Based on daily maps of fronts in the region they developed monthly composites of front frequency – front frequency is front probability divided by 100 – spanning 29 years for SST and 14 years for chlorophyll-a concentration (Chl). Although much of their analysis addressed fronts over a significant fraction of the CCS – their focus was on a comparison between SST and Chl fronts and generally at shorter time scales than of interest here – they did address long term trends in front frequency for a relatively small region encompassing the Ensenada front. This region is shown in Figure 3 and is the focus of the comparison between their work and ours discussed in this section.

Kahru et al. (2012) applied the SIED algorithm (the same algorithm described in Section 1.1, albeit with slightly different thresholds) to daytime 4-km AVHRR Pathfinder v5.0 and v5.1[4] data. These are earlier versions of the Pathfinder data than the version used in our analysis. Furthermore, Kahru et al. used a threshold of three digital counts between the means of the warm and cold populations in the histogram analysis (SIED) while we used a threshold of four. They may also have performed their analysis on the data as obtained from NODC, 0.01 K/digital count, compared with the 0.05 K/digital count scaled version that we used. This means that the minimum temperature difference between two populations in their case was either 0.03 K or 0.15 K compared with our 0.2 K. Finally, Kahru et al. required a minimum of ten pixels per segment while we required only five pixels. As a result, Kahru et al.

[4] The Pathfinder data available at the time of the Kahru et al. analysis was a mixture of v5. 0 and 5.1, v5.0 for 1985-2009 and v5.1 for 1981-1984.

(2012) will detect weaker fronts than we do, but they will have to be longer. These effects tend to compensate to some extent, especially in that weaker fronts are likely to be shorter. For this comparison we used daytime fields to be consistent with Kahru et al.

Kahru et al. determined front frequency by month for the Ensenada region by first dividing the number of daytime front pixels for the month at each pixel location by the number of clear pixels at the same location and then averaging, again by month, these front frequencies over all pixels in the Ensenada region (a 375 km diameter circle centered on 31.3°N; 120.2°W). As with Kahru et al., we only used pixels in the Ensenada region that had three or more clear observations for the month. The monthly mean front probability for the region was calculated by taking the mean of all pixel front probabilities within the domain. The monthly time series from these two analyses are shown in Figure 9; Kahru et al.'s results have been converted to probability for the purpose of this plot. Despite the differences both in the application of the detection algorithm and in the calculation of monthly probability the trends are quite similar. From 1981 through 1998, the two time series track each other quite well as they do following 2005. However, from 1998 through 2004, the time series of Kahru et al. is significantly noisier and the smoothed time series separate.

Kahru et al. also estimated the trend in Chl front frequency for the Ensenada region for the 16 years covered by the Sea-viewing Wide Field-of-view Sensor (SeaWiFS), Moderate-resolution Imaging Spectroradiometer (MODIS) Aqua, and the MEdium Resolution Imaging Spectrometer (MERIS), the sensors from which Chl data were obtained. This was done using the same configuration of SIED and front

frequency was calculated in the same fashion. The trend in Chl front frequency was found to be approximately twice that which they found in SST front frequency for the same 16-year period and to be statistically significant at the 99% confidence level, as was the trend in SST front frequency. Given that the Chl data was obtained from different sensors carried on different satellites, the statistically significant positive trend in front frequency found for this region supports the positive trend in front frequency found in SST.

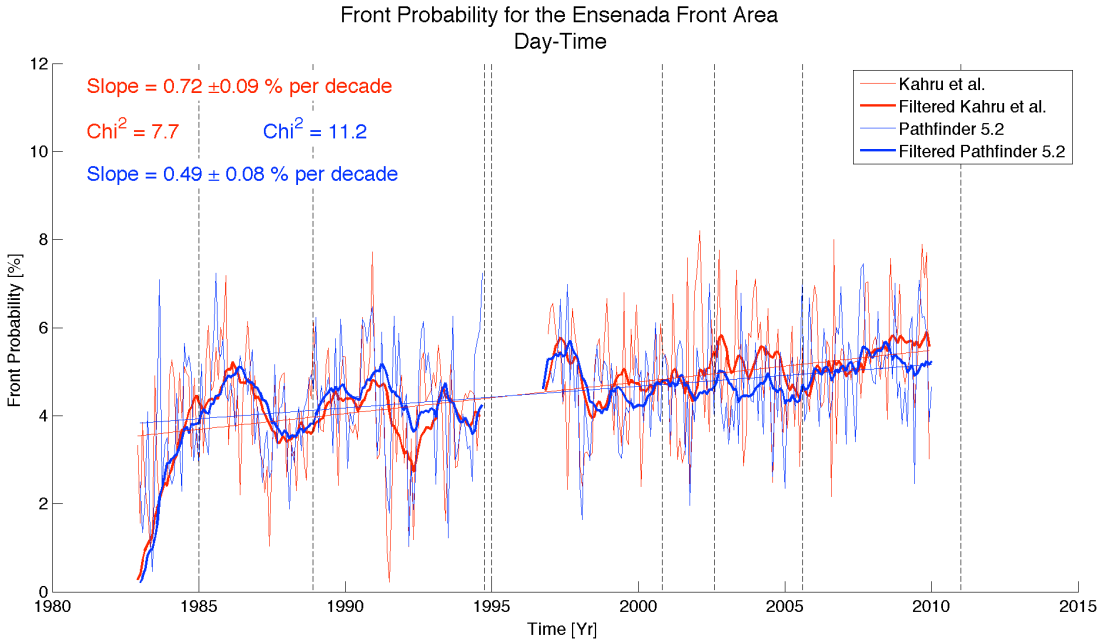

Figure 9. Monthly averaged daytime front probability within the Ensenada Front Region. The blue line was obtained using the Pathfinder v5.2 and the Red line was obtained from Kahru et al. (2012). The thin lines are the 12 month filtered time series.

1.3.2 Global Front Probability

Trends in global front probability were determined by first summing, for each nighttime image, the number of front pixels in all SIED windows between 80°N and 80°S with at least 90% of the pixels providing good SST values. The number of clear pixels were also summed for the same windows and these (front and clear) sums were then summed for all nighttime images in each month. Monthly global front probability was calculated from these sums (Figure 10). As noted in previous sections, SIED windows north of 80°N, between January 1995 and December 1995 and between July 2002 and July 2005 were excluded from this analysis. Also shown in Figure 10 is the least squares fit line to the monthly front probabilities. Nighttime front probability increases at a rate of 0.2410 ± 0.0174%/decade; this trend is statistically different from zero at the 95% confidence level (approximately two standard deviations of the uncertainty in the slope). The chi-squared value for a normal distribution of the residuals is 11.02. This is below the threshold value of 14.06; i.e., the residual values about the fit are normally distributed suggesting that a linear fit to the data is appropriate.

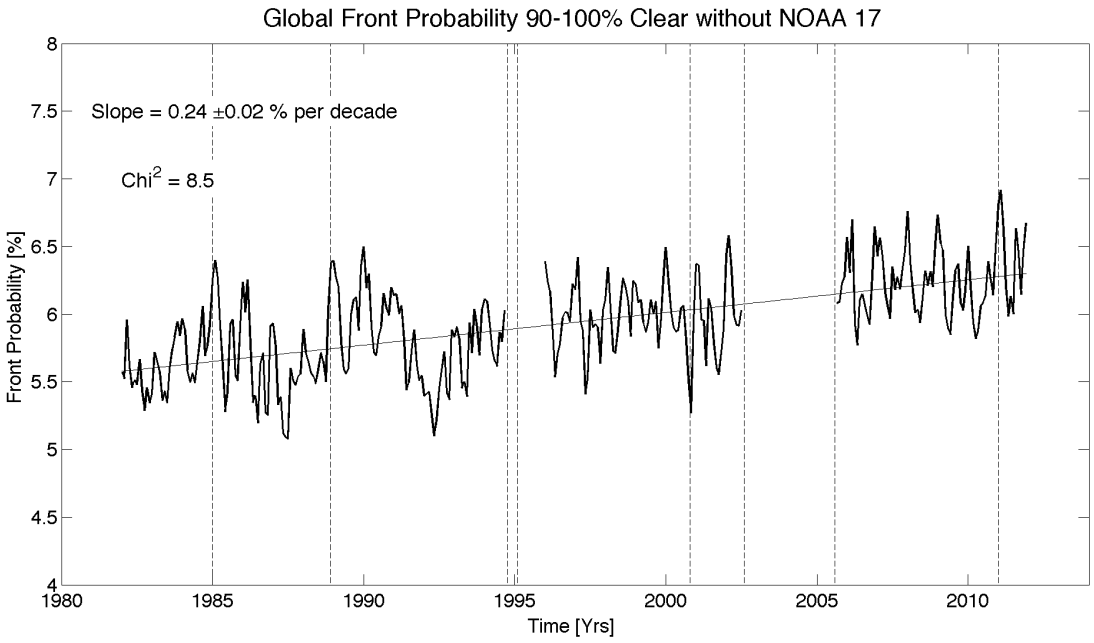

Figure 10. Global front probability based on SIED windows that are 90-100% clear. The thin black line is the linear regression of the global front probabilities to time. Vertical dashed lines delineate the range for each of the different sensors used in the time series.

1.3.3 Regional Analysis

The analysis presented in the previous section provides an estimate of the global trend in front probability, but says nothing about the spatial distribution of this trend; i.e., it is not clear how uniform the global trend is from region to region. More importantly, a change in the global distribution of clear pixels over the study period could alter the trend. For example, if the fraction of cloud cover over lower front probability regions increased over the course of the study with the fraction of cloud cover over the other regions remaining the same, the estimate of the trend in global front probability would be increased above its true value. For these reasons, we examine in this section the spatial distribution of trends in front probability. Front probability was determined for each 32x32 pixel by one month space time window for all SIED windows that were 90% or more clear excluding those north of 80°N, between January 1995 and December 1995 (the early NOAA-14 data) and between July 2002 and July 2005 (all of the NOAA-17 data). The temporal trend in monthly front probability was then determined by least squares fit of a straight line to the front probabilities in the time series for each SIED window. Figure 11 is a plot of the time series and best-fit straight line for an SIED window in the North East Atlantic near Africa (the star in Figure 3). The temporal trends at each location for which there were at least two monthly values in the 30-year time series are shown in Figure 12.

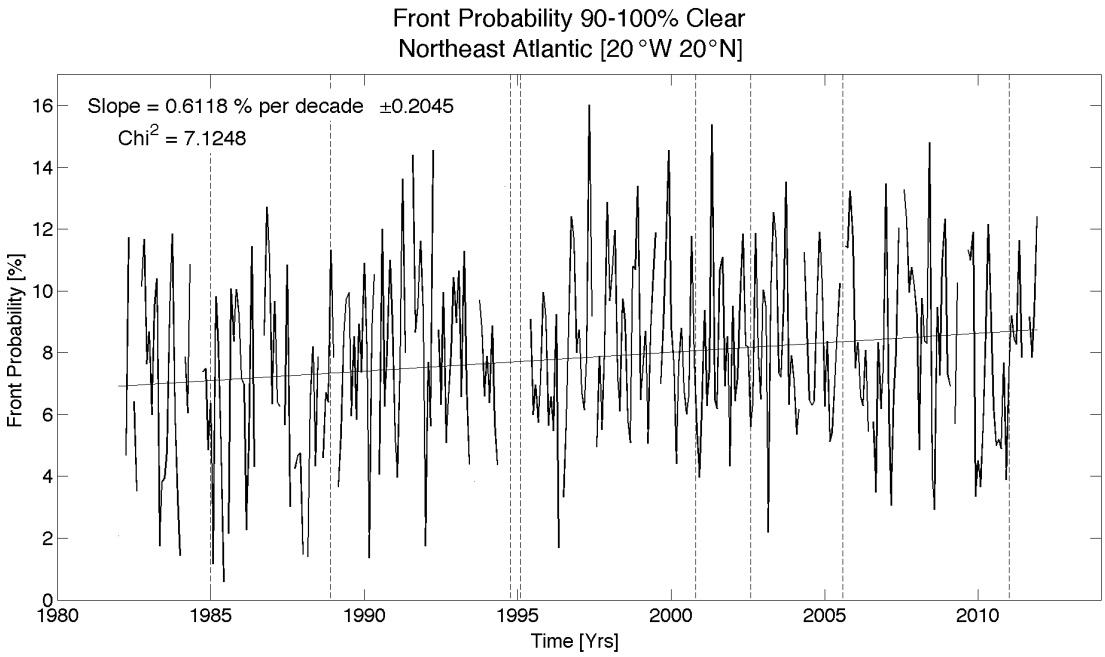

Figure 11. Example of the monthly front probability for a small region in the Northeast Atlantic (20°N; 20°W) using only times that were 90-100% clear within the SIED window.

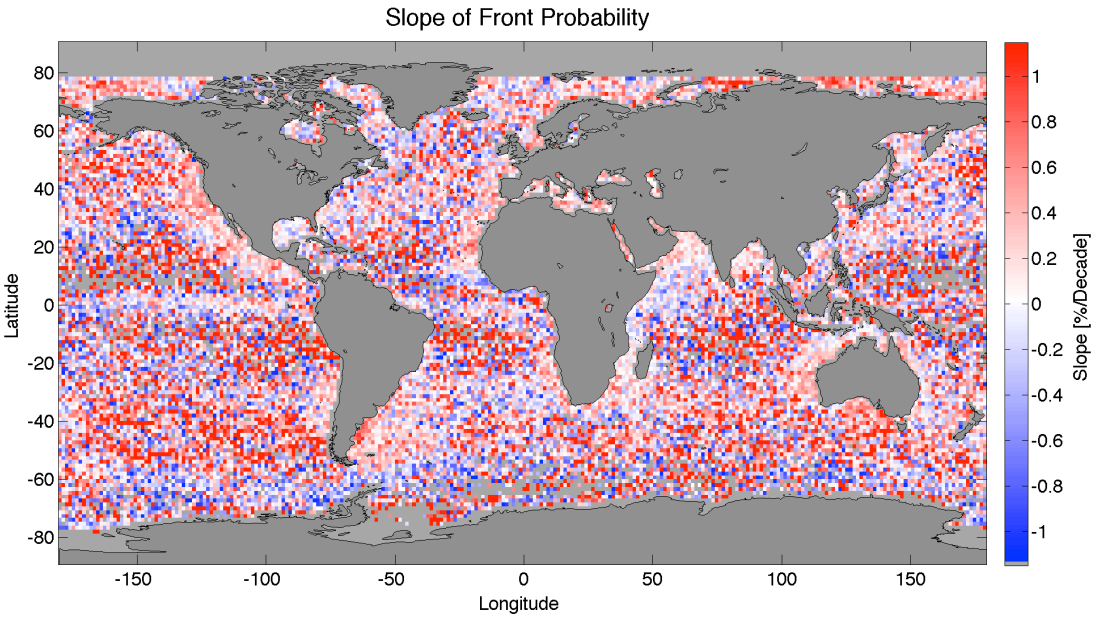

Figure 12. Slope of front probability.

Although a significant fraction of the slopes associated with the SIED windows shown in Figure 12 are statistically different from zero at the 95% confidence level (not shown explicitly), the temporal distribution of the data from which these slopes were generated is not clear. This is because the requirement that 90% or more of the pixels be clear in each SIED window results in the elimination of a number of the monthly probabilities in the time series; i.e., the trends shown in Figure 12 may result from a short interval in the overall time series or from a small number of months. In order to assure a relatively broad distribution in time, additional constraints were placed on the time series from which temporal trends in front probability were calculated with one set of constraints being applied to the entire, 360 month time series, and a second set to month of the year, the twelve 30-month time series – all Januarys, all Februarys, etc.

Analysis of the 12 monthly trends was undertaken to determine to what extent an annual signal in the trends might impact use of the entire time series to calculate the trends. Specifically, a bias might be introduced in the overall time series if there was a substantial difference in monthly trends and the months with good data tended to be at one end or the other of the time series. The additional temporal constraint applied to these time series was that at least 2 monthly front probability values be available in each of the three decades studied. The results of this analysis are presented in Table 2. The mean trends and the uncertainty of these means are quite similar from month to month suggesting that analysis of the entire series (for each SIED window), constrained as described below, will not be significantly impacted by the particular

months contributing to the time series. We therefore focus on the trend at each SIED window based on the entire time series in the remainder of this section.

	Total Number of Locations	Mean Slope (% / Year)	Standard Deviation (% / Year)
Entire Data Set (all months)	3923	0.016	0.039
January	1718	0.025	0.094
February	1695	0.025	0.096
March	2061	0.015	0.091
April	1946	0.018	0.087
May	1889	0.021	0.091
June	1843	0.019	0.094
July	2065	0.021	0.094
August	2310	0.019	0.089
September	1954	0.018	0.093
October	1487	0.018	0.090
November	1174	0.017	0.088
December	1307	0.022	0.092

Table 2. Statistics for the trends in front probability by month of year. Column 1 – the number of points that meet the temporal requirements; column 2 – the mean slope of the trend in front probability for the SIED windows that meet the temporal requirements; column 3 – the standard deviation of the slopes of column 2.

For the analysis of the entire time series only those SIED windows for which all but two of the 12[5] 2-year intervals had at least two monthly front probability values were used. The reason for excluding two of these 2-year intervals is somewhat arbitrary – the goal is to maximize the number of SIED windows with a trend while assuring a broad temporal coverage of the data. Excluding two 2-year intervals assured at least one monthly value in the final ten years of the time series. The 30-year trends

[5] Recall that 1995 and July 2002 to July 2005 are not included in the time series hence no requirements for data were made for the two-year periods overlapping these intervals; i.e., 1994-1995, 2002-2003, and 2004-2005.

for the SIED windows meeting this criterion are shown in Figure 13. The resulting field of trends in front probability is sparse in most open ocean areas. Not surprisingly, the SIED windows where there are values in Figure 13 closely matches locations that are relatively clear in Figure 2. With the exception of the equatorial region and a small fraction of the North and South Atlantic and Pacific subtropical convergences, there are virtually no regions in the open ocean meeting the temporal distribution requirement. This means that, although the slopes shown in Figure 12 are suggestive of trends, care must be taken in their interpretation because of the limited temporal extent of the time series used to estimate these trends. For this reason, in the remainder of this section, we focus on the constrained dataset shown in Figure 13.

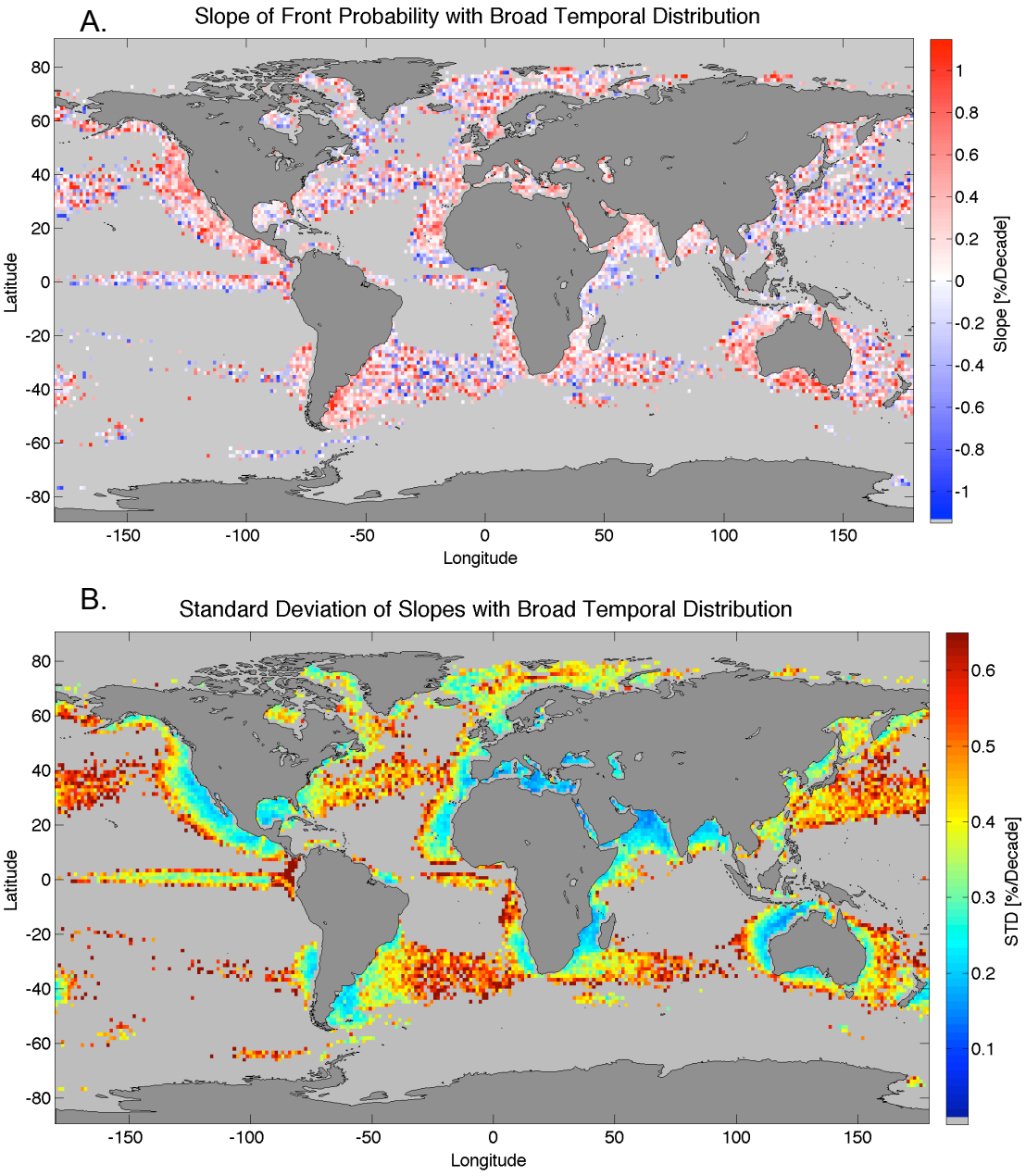

Figure 13. (A) Slope of front probability for time series meeting the temporal distribution requirement. (B) Standard error of the slopes shown in A.

The standard deviations of the slopes shown in Figure 13A are presented in Figure 13B. These were determined using the bootstrap method (Emery and Thomson, 2001). Note the relatively large standard deviations in all of the open ocean regions,

with the exception of the equatorial Pacific, and on the seaward edge of most of the coastal regions. Although all of these (large standard deviation) pixels passed the criterion applied to the temporal distribution of the data in the time series, the number of monthly values at locations with large standard deviations tended to be relatively low. Specifically, the number of monthly SIED windows contributing to the time series at locations with a standard deviation in excess of 0.035%/year is 87±24 and for windows with a standard deviation less than 0.030%/year is 195±64.

The mean trend for the data shown in Figure 13A is 0.26±0.019 %/decade with 77% of the trends being positive. This trend is consistent with the global trend obtained in the previous section and is statistically different from zero at the 95% confidence level. However, many of the individual trends are not statistically different from zero. Figure 14 shows those that are at the 95% confidence level.

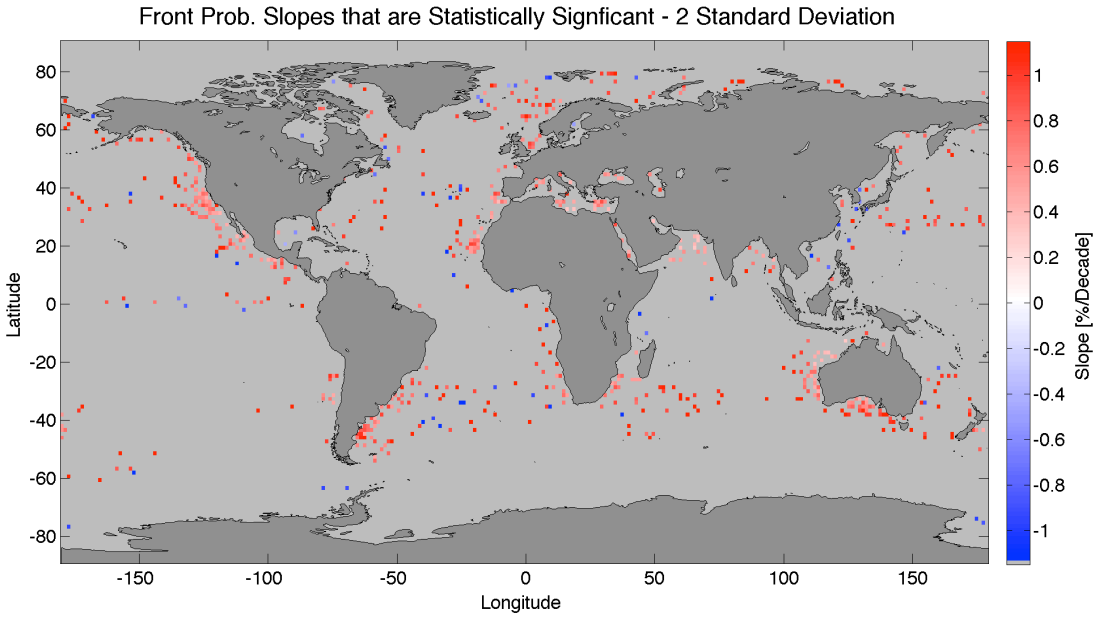

Figure 14. SIED windows with trends significantly different from zero at the 95% confidence level.

Of interest in this plot are the five areas with relatively dense clusters of SIED windows with statistically significant positive trends in front probability and the lack of any clusters of statistically significant negative trends. The clusters of positive trends are on the inner Patagonian Shelf, in the Great Australian Bight off of South Australia, the upwelling region off of West Australia, the upwelling region between 15º and 20ºN off the west coast of Africa and much of the west coast of North America from 10º to 40ºN.

The cluster of positive front probability trends off the west coast of North America includes the Ensenada front location of the study by Kahru et al. (2012). Kahru et al. suggested that both changes in upwelling associated with the warm/cold coastal SST and changes in the large-scale SST cross-shelf gradient may exert a direct control on the statistics of SST fronts on the scale of the California Current. They correlated the monthly coastal upwelling index in the California current system with the mean SST frontal frequency index to quantify the influence of upwelling winds on frontal frequency. A significant correlation exists between the winds and frontal frequency in the high-frequency bands of monthly timescales. However, on year-to-year timescales, they found that the frequency of SST fronts does not follow the changes in upwelling winds, but instead is correlated with changes in the large-scale cross-shelf gradient of SST (Kahru et al., 2012).

The regions of positive clusters off the west coasts of Africa and Australia correspond to upwelling regions similar to that off the coast of California hence one might argue that the mechanisms proposed by Kahru et al. (2012) apply here as well. Although not an upwelling region, the region on the inner Patagonian Shelf is in an

extremely rich biological environment (Belkin et al., 2009; Alemany et al., 2009). In that fronts play a significant role in biological activity, changes in the number or strength of fronts could well play a significant role in the biological activity in this area.

Finally, although much more speculative, we note that in the South Pacific from approximately 180°W to the coast of South America and between 30°S and 60°S, there are significantly more positive trends than negative trends (Figure 12) suggesting that this might also be a region of enhanced front probability.

1.4 Conclusions

We have performed a systematic quantitative study of global front probability on the 30-year time series of global Pathfinder v5.2 4km SST fields. Because of the impact of cloud cover on the front detection algorithm, only regions that were substantially clear (90 to 100%) were used for this study. On average, front probability has been increasing globally at a very nearly linear rate of approximately 0.25 %/decade; i.e., over the 30-year record the mean probability of finding a front with the SIED algorithm in Pathfinder v5.2 data has increased from approximately 5.58% to 6.30%. However, the trend in front probability is not globally uniform so the study also includes a determination of the regional trends in front probability. Because of the desire to ensure a relatively broad temporal distribution in the SIED windows used to calculate trends in front probability, this portion of the analysis yielded results only within an approximately 750 km band of the continents. This analysis showed clusters of positive trends that were significantly larger than the mean trend, typically in the 0.6 to 0.8%/decade range resulting in a 30 to 50% increase in the number of fronts over the past 30 years. A significant fraction of these clusters are found in regions of strong upwelling. Bakun (1990) proposed that global greenhouse warming would lead to intensification of continental thermal lows in regions adjacent to upwelling. The amplification of the low would increase onshore-offshore atmospheric-pressure gradients; amplify alongshore winds therefore accelerating coastal upwelling circulation. García-Reyes et al. (2010) used 25 years of buoy data to confirm Bakun's hypothesis and found a clear trend toward stronger upwelling off California. In that

upwelling regions are often regions of enhanced front probability (Figure 3), it is not surprising that an increase in upwelling results in an increase in front probability.

There are a number of factors that affect front detection with the SIED algorithm. We have attempted to correct for these or to restrict their impact on our results by restricting the data that we used in the analyses. This resulted in much less global coverage than we would have liked without completely removing the concern that we have missed a non-geophysical contribution to the trend. The fact that Kahru et al. (2012) found a similar trend in satellite-derived chlorophyll-a as they did in SST data for the period of overlap between the datasets lends credence to the trends discussed herein. This approach, using satellite-derived chlorophyll-a data as well as SST data from other satellites would help to strengthen the results of this study.

We believe that trends for some regions eliminated in this analysis could be determined by increasing the size of the regions used in the open ocean and correcting for cloud cover allowing for the use of SIED windows with a larger fraction of cloud cover. Use of geostationary data for other regions in the ocean would also allow for regional estimates of the daily signal in front probability allowing for a correction in orbital drift and possibly the inclusion of the NOAA-17 data not used in this analysis.

Finally, we note that the AVHRR data stream is going to be reprocessed as part of the Pathfinder effort. The problem of values where there is a retrieval being set to -1, discussed in Section 1.2.2, will be addressed in the reprocessing. This will allow for the recovery of fronts that are masked by the variance test.

Bibliography

Alemany, D., Acha, E. M., & Iribarne, O. (2009). The relationship between marine fronts and fish diversity in the Patagonian Shelf Large Marine Ecosystem. *Journal of Biogeography*, *36*(11), 2111-2124.

Bakun, A. (1990). Global climate change and intensification of coastal ocean upwelling. *Science*, 247(4939), 198-201.

Belkin, I. M., Cornillon, P. C., & Sherman, K. (2009). Fronts in large marine ecosystems. *Progress in Oceanography*, 81(1), 223-236.

Capet, X., McWilliams, J. C., Molemaker, M. J., & Shchepetkin, A. F. (2008). Mesoscale to submesoscale transition in the California Current System. Part II: Frontal processes. *Journal of Physical Oceanography*, 38(1), 44-64.

Cayula, J. F., & Cornillon, P. (1992). Edge detection algorithm for SST images. *Journal of Atmospheric and Oceanic Technology*, 9(1), 67-80.

Cayula, J. F., & Cornillon, P. (1995). Multi-image edge detection for SST images. *Journal of Atmospheric and Oceanic Technology*, 12(4), 821-829.

Chelton, D. B., Esbensen, S. K., Schlax, M. G., Thum, N., Freilich, M. H., Wentz, F. J., Gentemann, C. L., McPhaden, M. J., and Schopf, P. S. (2001). Observations of Coupling between Surface Wind Stress and Sea Surface Temperature in the Eastern Tropical Pacific. *Journal of Climate,* 14 (7), 1479-1498.

D'Asaro, E., Lee, C., Rainville, L., Harcourt, R., & Thomas, L. (2011). Enhanced turbulence and energy dissipation at ocean fronts. *Science*, 332(6027), 318-322.

Evans, B. (2013): personal communication.

Emery, W. J., & Thomson, R. E. (Eds.). (2001). *Data analysis methods in physical oceanography*. Elsevier Science, 295-301.

Ferrari, R. (2011). A frontal challenge for climate models. *Science*, 332(6027), 316-317.

Fox-Kemper, B., Danabasoglu, G., Ferrari, R., Griffies, S. M., Hallberg, R. W., Holland, M. M., Maltrud, M. E., Peacock, S., and Samuels, B. L. (2011). Parameterization of mixed layer eddies. III: Implementation and impact in global ocean climate simulations. *Ocean Modelling*, 39(1), 61-78.

García-Reyes, M., & Largier, J. (2010). Observations of increased wind-driven coastal upwelling off central California. *Journal of Geophysical Research*, *115*(C4), C04011.

Howe, P., P. C. Cornillon, and D. S. Ullman (2013). Sea-surface temperature front probability statistics produced by regional edge detection algorithms. *In preparation*, 1-25.

Ignatov, A., Laszlo, I., Harrod, E. D., Kidwell, K. B., & Goodrum, G. P. (2004). Equator crossing times for NOAA, ERS and EOS sun-synchronous satellites. *International Journal of Remote Sensing*, 25(23), 5255-5266.

Kahru, M., Di Lorenzo, E., Manzano-Sarabia, M., & Mitchell, B. G. (2012). Spatial and temporal statistics of sea surface temperature and chlorophyll fronts in the California Current. *Journal of plankton research*, 34(9), 749-760.

Kilpatrick, K. A., Podesta, G. P., & Evans, R. (2001). Overview of the NOAA/NASA advanced very high resolution radiometer Pathfinder algorithm for sea surface temperature and associated matchup database. *Journal of Geophysical Research*, *106*(C5), 9179-9197.

Le Fevre, J. (1986). Aspects of the biology of frontal systems. *Advances in Marine Biology*, 23, 163-299.

Liu, T. W., Xie, X., Polito, P. S., Xie, S. P., & Hashizume, H. (2000). Atmospheric manifestation of tropical instability wave observed by QuikSCAT and Tropical Rain Measuring Mission. *Geophysical research letters*, 27(16), 2545-2548.

Longhurst, A.R., (2010). *Ecological Geography of the Sea*, second edition. Academic Press, New York, NY. 560 pp.

Merchant, C. J., Embury, O., Rayner, N. A., Berry, D. I., Corlett, G. K., Lean, K., Veal, K. L., Kent, E. C., Llewellyn-Jones, D. T., Remedios, J. J., and Saunders, R. (2012). A 20 year independent record of sea surface temperature for climate from Along-Track Scanning Radiometers. *Journal of Geophysical Research: Oceans (1978–2012)*, 117(C12).

Molemaker, M. J., McWilliams, J. C., & Capet, X. (2010). Balanced and unbalanced routes to dissipation in an equilibrated Eady flow. *Journal of Fluid Mechanics*, 654, 35.

Norris, J. R. (2005). Multidecadal changes in near-global cloud cover and estimated cloud cover radiative forcing. *Journal of Geophysical Research: Atmospheres (1984–2012),* 110(D8).

Olson, D. B., Hitchcock, G. L., Mariano, A. J., Ashjian, C. J., Peng, G., Nero, R. W., & Podesta, G. P. (1994). Life on the edge: marine life and fronts. *Oceanography*, 7(2), 52-60.

Park, K.-A., Cornillon, P.C. & Codiga, D.L., (2006). Modification of surface winds near ocean fronts: Effects of Gulf Stream rings on scatterometer (QuikSCAT, NSCAT) wind observations. Journal Of Geophysical Research-Oceans, 111(C3), C03021.

Salter, J. (2013): Personal Communication on the effects of diurnal warming on sea surface temperature fronts.

Small, R. J., DeSzoeke, S. P., Xie, S. P., O'Neill, L., Seo, H., Song, Q., ... & Minobe, S. (2008). Air–sea interaction over ocean fronts and eddies. *Dynamics of Atmospheres and Oceans*, 45(3), 274-319.

Solomon, S., D. Qin, M. Manning, M. Marquis, K. Averyt, M. M. B. Tignor, H. L. J. Miller, and Z. Chen (Eds.) (2007). *Climate Change 2007*. The Physical Science Basis: Contributions of Working Group I to the Fourth Assessment Report of the Intergovernmental Panel on Climate Change. Cambridge University Press.

Song, Q., Cornillon, P., & Hara, T., (2006). Surface wind response to oceanic fronts. *Journal Of Geophysical Research*: *Oceans*, 111(C12), C12006.

Thomas, L. N., Tandon, A., & Mahadevan, A. (2008). Submesoscale processes and dynamics. *Ocean modeling in an eddying regime*, 17-38.

Ullman, D. S., & Cornillon, P. C. (1999). Satellite-derived sea surface temperature fronts on the continental shelf off the northeast US coast. *Journal of Geophysical Research: Oceans (1978–2012)*, 104(C10), 23459-23478.

Young, I. R., Zieger, S., & Babanin, A. V. (2011). Global trends in wind speed and wave height. *Science*, *332*(6028), 451-455.